Regular Article

Enhanced nanoparticle detection with liquid droplet resonators

M.R. Foreman[1,a], S. Avino[2], R. Zullo[2], H.-P. Loock[3], F. Vollmer[1], and G. Gagliardi[2]

[1] Max-Planck-Institute for the Science of Light, Laboratory of Nanophotonics and Biosensing, Günther-Scharowsky-Straße 1, 91058 Erlangen, Germany
[2] Consiglio Nazionale delle Ricerche, Istituto Nazionale di Ottica (INO), via Campi Flegrei 34 – Comprensorio A. Olivetti, 80078 Pozzuoli, Naples, Italy
[3] Department of Chemistry, Queen's University, Kingston, K7L 3N6, Ontario, Canada

Abstract. Whispering gallery mode particle sensing experiments are commonly performed with solid resonators, whereby the sensing volume is limited to the weak evanescent tail of the mode near the resonator surface. In this work we discuss in detail the sensitivity enhancements achievable in liquid droplet resonators wherein the stronger internal fields and convenient means of particle delivery can be exploited. Asymptotic formulae are derived for the relative resonance shift, line broadening and mode splitting of TE and TM modes in liquid droplet resonators. As a corollary the relative fraction of internal and external mode energy follows, which is shown to govern achievable sensitivity enhancements of solute concentration measurements in droplet sensors. Experimental measurements of nanoparticle concentration based on whispering gallery mode resonance broadening are also presented.

1 Introduction

Dielectric optical microresonators have attracted considerable interest in recent years [1–4], since they can exhibit ultra-low loss modes, commonly known as whispering gallery modes (WGMs), in which electromagnetic waves are guided by total internal reflection around a circumference close to the surface of the resonator. Low losses, and the associated high quality factors $Q > 10^9$, imply the intracavity photon lifetime is long, that is to say light coupled into a WGM circulates for a long time before ultimately being lost via scattering or absorption. The highest quality factors observed to date were achieved using silica microspheres [5,6] and crystalline CaF_2 disc resonators [7], however, an abundance of alternative geometries have also been investigated, including ring, toroidal, bottle-neck, goblet, microbubble and capillary resonators [8–16].

The intrinsically high Q factors and small modal volumes afforded by WGMs make them interesting for a wide range of applications, such as microlasers, optical frequency comb generation, add-drop elements, novel light sources and fundamental

---

[a] e-mail: matthew.foreman@mpl.mpg.de
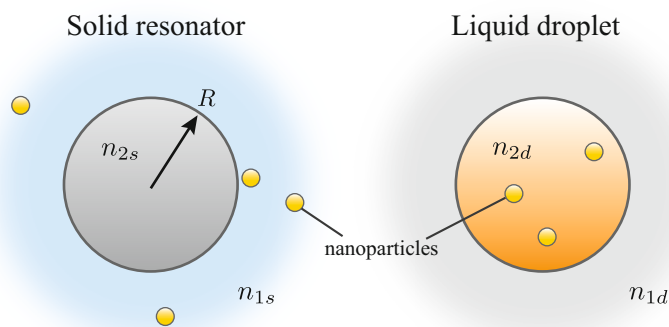
Fig. 1. Schematic depiction of solid WGM resonators as compared to liquid droplet resonators.

cavity quantum electrodynamical studies [17–21]. Furthermore, due to their extreme sensitivity to refractive index changes and optical absorption of the surrounding environment and resonator material itself, WGMs are also seeing use in chemical [22,23] and biological sensors [1,4,24,25]. For example, Vollmer et al. recently examined the use of silica microspheres for detection of proteins and viruses [24,26]. By measuring the shift in WGM resonance frequency they observed proteins binding to the sphere and their theoretical calculations have shown that single molecule detection is feasible [27]. Interferometric methods have, moreover, been employed to detect nanoparticles attached to a microtoroidal resonator [28,29], whilst plasmonic enhancements have also seen recent attention [30–32]. The reader is referred to recent reviews of WGM sensing for further examples and historical details [1,2,33].

Solid microresonators, however, suffer from a number of problems. Of particular significance is that the majority of the WGM energy lies within the resonator, implying particles can only interact with the relatively weak evanescent tail in the external medium. The magnitude of induced resonance perturbations, such as resonance shifts, are comparatively small as a result. Furthermore, delivery of analyte to the sensing region frequently relies on particle diffusion, such that long measurement times may be required before a detection event is recorded. Moreover, in applications in which concentration, as opposed to single particle, measurements are desired, saturation of surface binding sites or attainment of surface equilibrium conditions is required, hence also leading to slow measurements.

Use of a liquid droplet as a WGM microresonator offers a number of benefits to help overcome these issues. Firstly, the analyte can easily be incorporated into the droplet material, such that the liquid droplet simultaneously serves as sensor and sample (see Fig. 1). In this way, analyte particles interact with the stronger portion of the WGM leading to a higher detection sensitivity [34]. Furthermore, equilibrium conditions are not required for many particle measurements, therefore improving measurement times. Droplet resonators can also be easily created without the need for complex fabrication procedures, whilst surface tension ensures the resonator surface is free of surface roughness. Surface scattering losses are hence only limited by thermal fluctuations of the surface, thus leading to high Q factors. Furthermore, liquid droplet resonators lend themselves to integration with microfluidic analyte delivery schemes and use on microfluidic analysis platforms, when combined with free space coupling techniques [35]. Despite these potential advantages, no experimental demonstration of droplet based WGM chemical detection was reported until recently, except for the work of Kiraz and coworkers who examined "surface-standing" glycerol drops doped

with dye molecules for lasing experiments [17,18]. Indeed, it is only in a very recent separate experiment, that some of the current authors have reported the first proof-of-concept demonstration of liquid droplet WGM resonators as chemical sensors [34].

In this paper we provide theoretical predictions as to the potential sensitivity enhancements achievable using a liquid droplet cavity relative to a solid dielectric resonator for different sensing modalities. Moreover, we provide a first comparison between theory and experimental measurements of WGM line broadening caused by gold nanoparticles. In Sect. 2 we therefore briefly recall some useful properties of WGM resonances in spherical cavities. A number of asymptotic formulae are subsequently derived pertaining to the total mode energy and confinement. Section 3 proceeds to derive asymptotic results for the relative enhancement in particle induced frequency shifts in liquid droplet WGM resonators. Line broadening and WGM splitting schemes are also considered, before the sensitivity gains for analyte concentration measurements are given. An experimental demonstration of a droplet cavity sensor wherein gold nanoparticles are introduced and the resulting linewidth perturbations observed and compared with theoretical prediction, is then presented in Sect. 4.

2 Definition and properties of whispering gallery modes

Resonant properties of spherical microcavities can be treated within the analytic framework of Debye-Mie theory, the details of which can be found in many classical textbooks, e.g. [36,37]. For our derivations it is useful, however, to recall a number of properties of such resonances here. In particular, it can be shown that for a microsphere of radius R, discrete resonances occur at frequencies $\omega = kc$, satisfying the condition

$$\frac{\left[n_1 kR\, h_l(n_1 kR)\right]'}{h_l(n_1 kR)} = \mathcal{N}^\nu \frac{\left[n_2 kR\, j_l(n_2 kR)\right]'}{j_l(n_2 kR)}, \tag{1}$$

where $k = 2\pi/\lambda$, λ is the optical wavelength, c is the speed of light, $n_{1,2}$ is the refractive index of the host medium and microsphere respectively (see Fig. 1), prime notation denotes differentiation with respect to the argument of the spherical Bessel and Hankel functions (of the first kind), $j_l(z)$ and $h_l(z)$, and $\mathcal{N}^{\text{TE}} = 1$ or $\mathcal{N}^{\text{TM}} = (n_1/n_2)^2$ for transverse electric ($\nu = \text{TE}$) or transverse magnetic ($\nu = \text{TM}$) modes respectively. Note that we assume isotropic media such that we can neglect non-transverse modes and that for a mode of given order $l = 1, 2, \ldots$, multiple solutions to Eq. (1) exist, corresponding to different azimuthal and radial orders, as can be indexed by the additional mode indices $m = -l, -l+1, \ldots, l$ and $p = 1, 2, \ldots$.

Equation (1) follows by enforcing continuity of the tangential components of the electric and magnetic fields inside and outside the microsphere at the resonator surface. Accordingly, the associated electric field distributions for each mode, expressed in spherical polar field components $\mathbf{E} = (E_r, E_\theta, E_\phi)$, and assuming non-magnetic media, are given by

$$\mathbf{E}^{\text{TE}}_{lmp}(\mathbf{r}) = A_j^{\text{TE}} \omega \mu_0 \begin{bmatrix} 0 \\ -\frac{m}{\sin\theta} f_l^j(n_j kr) Y_{lm}(\theta,\phi) \\ -i f_l^j(n_j kr) \frac{\partial}{\partial\theta} Y_{lm}(\theta,\phi) \end{bmatrix} \tag{2}$$

and

$$\mathbf{E}^{\text{TM}}_{lmp}(\mathbf{r}) = A_j^{\text{TM}} \begin{bmatrix} l(l+1)\frac{f_l^j(n_j kr)}{r} Y_{lm}(\theta,\phi) \\ \frac{1}{r}\frac{d}{dr}\left[r f_l^j(n_j kr)\right] \frac{\partial}{\partial\theta} Y_{lm}(\theta,\phi) \\ \frac{im}{\sin\theta}\frac{1}{r}\frac{d}{dr}\left[r f_l^j(n_j kr)\right] Y_{lm}(\theta,\phi) \end{bmatrix}, \tag{3}$$

where μ_0 is the permeability of free space, $f_l^j(z) = h_l(z)$ for $j = 1$ (i.e. outside the microsphere, $r \geq R$) and $f_l^j(z) = j_l(z)$ for $j = 2$ (within the microsphere, $r \leq R$). The choice of $f_l^j(z)$ is determined by requiring satisfaction of the radiation condition at infinity, and a physical, i.e. non-divergent, field at the resonator center. Furthermore, $Y_{lm}(\theta, \phi) = c_{lm} P_l^m(\cos\theta) \exp[im\phi]$ are the spherical harmonic functions, $c_{lm} = [(2l+1)(l-|m|)!]^{1/2}/[4\pi(l+|m|)!]^{1/2}$ and $P_l^m(\cos\theta)$ are the associated Legendre polynomials. Adopting the mode normalisation whereby $A_2^\nu = 1$ ($\nu = $ TE, TM) and letting $z_j = n_j kR$, continuity of the transverse field components, E_θ and E_ϕ, implies

$$A_1^{\mathrm{TE}} = \frac{j_l(z_2)}{h_l(z_1)} \quad \text{and} \quad A_1^{\mathrm{TM}} = \frac{[z_2 j_l(z_2)]'}{[z_1 h_l(z_1)]'} = \frac{n_2^2}{n_1^2} \frac{j_l(z_2)}{h_l(z_1)}, \tag{4}$$

where the latter equality for the TM case follows from Eq. (1).

Given the results above it is possible to determine the total electric energy of a single resonant mode as given by

$$U_{lmp}^\nu = \frac{1}{2}\epsilon_0 \left[n_1^2 \int_0^{2\pi} \int_0^\pi \int_R^\infty \left| \mathbf{E}_{lmp}^\nu(\mathbf{r}) \right|^2 r^2 \sin\theta \, dr \, d\theta \, d\phi \right.$$
$$\left. + n_2^2 \int_0^{2\pi} \int_0^\pi \int_0^R \left| \mathbf{E}_{lmp}^\nu(\mathbf{r}) \right|^2 r^2 \sin\theta \, dr \, d\theta \, d\phi \right], \tag{5}$$

where ϵ_0 is the permittivity of free space. Evaluation of the first (exterior) integral in Eq. (5), however, requires care because it is divergent. In the literature, this problem has been previously overcome, for example, using a convergence coordinate [38] or via a reformulation in terms of a volume and surface integral [39], however, here we adopt the more physically motivated approach of Chowdhury et al. [40]. Specifically, since we are concerned with only the bound components of the mode, as opposed to the radiating components, we can approximate the mode energy by performing the exterior integral only over the region in which the evanescent field dominates. Accordingly, we modify the radial integration domain to $r \in [R, R_0]$, where R_0 represents the first zero of the spherical Neumann function $y_l(n_1 kr)$.

The angular integrals of Eq. (5) can be easily performed using the result [41]

$$\int_0^\pi \left[\frac{m^2}{\sin^2\theta} P_l^m(\cos\theta)^2 + \left(\frac{d}{d\theta} P_l^m(\cos\theta) \right)^2 \right] \sin\theta \, d\theta = \frac{l(l+1)}{2\pi c_{lm}^2} \cdot \tag{6}$$

Determination of the mode energy, therefore, reduces to evaluation of the set of radial integrals:

$$I_j^{\mathrm{TE}} = \int_{r_{1j}}^{r_{2j}} r^2 [f_l^j(n_j kr)]^2 \, dr \tag{7}$$

$$I_j^{\mathrm{TM}} = \int_{r_{1j}}^{r_{2j}} l(l+1)[f_l^j(n_j kr)]^2 + \left[\frac{d}{dr} \left[r f_l^j(n_j kr) \right] \right]^2 \, dr \tag{8}$$

where now we take $f_l^1(z) \approx y_l(z)$ since for high order modes ($l \gg 1$), such as WGMs, the spherical Hankel function is dominated by the contribution from the Neumann function for $R \lesssim R_0$. We also note $r_{11} = r_{22} = R$, $r_{12} = 0$ and $r_{21} = R_0$. Evaluation of the TE integrals (Eq. (7)) can be immediately performed analytically (see e.g. [42]) yielding

$$I_1^{\mathrm{TE}} = -\frac{R^3}{2} y_l(z_1)^2 \left[1 - \frac{y_{l-1}(z_1) y_{l+1}(z_1)}{y_l(z_1)^2} \right] - \frac{R_0^3}{2} y_{l-1}(n_1 kR_0) y_{l+1}(n_1 kR_0) \tag{9}$$

$$I_2^{\text{TE}} = \frac{R^3}{2} j_l(z_2)^2 \left[1 - \frac{j_{l-1}(z_2)j_{l+1}(z_2)}{j_l(z_2)^2} \right]. \tag{10}$$

For high order modes we can also make the further approximation $y_{l\pm1}(n_1 k R_0) \approx 0$. Evaluation of the integrals I_j^{TM} is more involved and requires use of the recursion relations [43]

$$j_{l-1}(z) + j_{l+1}(z) = \frac{2l+1}{z} j_l(z), \tag{11}$$

$$l j_{l-1}(z) - (l+1) j_{l+1}(z) = (2l+1) j_l'(z), \tag{12}$$

(and similarly for $y_l(z)$) to transform Eq. (8) to read

$$I_j^{\text{TM}} = \frac{n_j^2 k^2}{2l+1} \left[(l+1) \int_{r_{1j}}^{r_{2j}} r^2 [f_{l-1}^j(n_j kr)]^2 dr + l \int_{r_{1j}}^{r_{2j}} r^2 [f_{l+1}^j(n_j kr)]^2 dr \right]. \tag{13}$$

Both integrals in Eq. (13) are of equivalent form to Eq. (7) and can hence be individually evaluated, yielding results analogous to Eqs. (9) and (10), such that

$$I_1^{\text{TM}} \approx -\frac{n_1^2 k^2 R^3}{2} y_l^2(z_1) \left[1 + \left(\frac{y_l'(z_1)}{y_l(z_1)} \right)^2 + \frac{3}{z_1} \frac{y_l'(z_1)}{y_l(z_1)} - \frac{(l-1)(l+2)}{z_1^2} \right] \tag{14}$$

$$I_2^{\text{TM}} = \frac{n_2^2 k^2 R^3}{2} j_l^2(z_2) \left[1 + \left(\frac{j_l'(z_2)}{j_l(z_2)} \right)^2 + \frac{3}{z_2} \frac{j_l'(z_2)}{j_l(z_2)} - \frac{(l-1)(l+2)}{z_2^2} \right] \tag{15}$$

where, again, factors such as $y_{l\pm1}(n_1 k R_0)$ are assumed to be negligible and the recursion relations (11) and (12) have been further employed to express the result in terms of derivatives of the spherical Bessel and Neumann functions.

Combining Eqs. (2)–(8) we can express the mode energy in the form

$$U_{lmp}^{\text{TE}} = \frac{\epsilon_0}{2} (1 + \mathcal{R}^{\text{TE}}) n_2^2 \omega^2 \mu_0^2 l(l+1) I_2^{\text{TE}} \tag{16}$$

$$U_{lmp}^{\text{TM}} = \frac{\epsilon_0}{2} (1 + \mathcal{R}^{\text{TM}}) n_2^2 l(l+1) I_2^{\text{TM}} \tag{17}$$

where $\mathcal{R}^\nu = (n_1^2/n_2^2)(I_1^\nu/I_2^\nu)|A_1^\nu|^2$ represents the relative fraction of electric energy stored in the host medium to that stored within the microsphere. Eqs. (9), (10), (14) and (15) can then be directly substituted into Eqs. (16) and (17) to yield the total electrical energy.

Simpler expressions for the mode energy can, however, be found if an asymptotic ($l \gg 1$) approximation is made. The results of such an approximation, when considering only the interior mode energy, are presented in [44] for TE modes only. We extend these results here and provide expressions for both TE and TM modes and also include the exterior field energy, which can be significant when the microsphere and host medium have a low refractive index contrast. To do so, it is necessary to note that an analogy can be drawn between the governing equations of morphological dependent resonances in a sphere and the quantum mechanical radial Schrödinger equation for a system of energy E and potential V_T [45]. In particular the analogy requires $E = n_j^2 k^2$ and the total potential (including the centrifugal barrier) is $V_T = k^2(n_1^2 - n_j^2) + l(l+1)/r^2$. Drawing the analogy with the classical resonance case we choose the decaying form of the radial function, i.e. consider $\psi(r) \sim y_l(n_1 kr) \sim \exp[-n_1 k\beta r]$ for $r \geq R$. The local wavevector follows by considering $\beta^2 = E - V_T$ [45] yielding $n_1^2 k^2 \beta^2 = n_1^2 k^2 - l(l+1)/r^2$ such that

$$\frac{y_l'(z_1)}{y_l(z_1)} \approx -\frac{\beta \exp[-\beta z_1]}{\exp[-\beta z_1]} = -\left[\frac{l(l+1)}{z_1^2} - 1 \right]^{1/2}. \tag{18}$$

Substituting Eq. (18) into the resonance condition (Eq. (1)) for TE and TM modes yields, after some minor algebraic manipulations,

$$\frac{j_l'(z_2)}{j_l(z_2)} \approx \begin{cases} -\frac{n_1}{n_2}\left[\frac{l(l+1)}{z_1^2} - 1\right]^{1/2} & \text{for TE modes} \\ \frac{1}{z_2}\left[\frac{n_2^2}{n_1^2} - 1\right] - \frac{n_2}{n_1}\left[\frac{l(l+1)}{z_1^2} - 1\right]^{1/2} & \text{for TM modes} \end{cases}. \tag{19}$$

Ultimately, it can then be shown from Eqs. (10)–(12), (15), (18) and (19) that

$$I_2^{\text{TE}} \approx \frac{R^3}{2} j_l(z_2)^2 \left[1 - \frac{n_1^2}{n_2^2} - \frac{n_1}{n_2 z_2}\left(\frac{l(l+1)}{z_1^2} - 1\right)^{1/2}\right] \tag{20}$$

$$\approx \frac{R^3}{2} j_l(z_2)^2 \left[\frac{n_2^2 - n_1^2}{n_2^2}\right] \tag{21}$$

and

$$I_2^{\text{TM}} = \frac{R^3}{2} j_l^2(z_2) n_2^2 k^2 \left[1 + \frac{n_2^2}{n_1^2}\left(\frac{l(l+1)}{z_1^2} - 1\right) + \frac{1}{z_2^2}\left(\frac{n_2^2}{n_1^2}\frac{n_1^2 + n_2^2}{n_1^2} - l(l+1)\right)\right.$$
$$\left. - \frac{n_2\left(n_1^2 + 2n_2^2\right)}{n_1^3 z_2}\left(\frac{l(l+1)}{z_1^2} - 1\right)^{1/2}\right] \tag{22}$$

$$\approx \frac{R^3}{2} j_l^2(z_2) n_2^2 k^2 \left[\frac{n_2^2 - n_1^2}{n_1^2}\right]\left[\frac{l(l+1)}{z_1^2}\frac{n_2^2 + n_1^2}{n_2^2} - 1\right], \tag{23}$$

where the latter equalities follow by noting the asymptotic result $z_2 \gg 1$ and $z_2 \sim \sqrt{l(l+1)}$, such that terms $O(z_2^{-1})$ (and larger negative powers) are dropped, whilst terms $O(1)$ e.g. $l(l+1)/z_2^2$ are retained. The explicit replacement $l(l+1) \to z_2^2$ was not made here (see below). It also follows that the relative fraction of energy outside and inside the microsphere is given by

$$\mathcal{R}^{\text{TE}} \approx \frac{n_1^2}{(n_2^2 - n_1^2)z_1}\left(\frac{l(l+1)}{z_1^2} - 1\right)^{1/2} \tag{24}$$

$$\mathcal{R}^{\text{TM}} \approx \frac{3n_1^2}{(n_2^2 - n_1^2)\,z_1}\left(\frac{l(l+1)}{z_1^2} - 1\right)^{1/2} \left/ \left(\frac{l(l+1)}{z_1^2}\frac{\left(n_1^2 + n_2^2\right)}{n_2^2} - 1\right)\right. . \tag{25}$$

We note a close similarity with expressions derived in [46]. Finally, we note that in the work of Lam et al. [42] the further replacement $l(l+1) \to z_2^2$ was made. In the cases considered in this article this was found to be a poor approximation, especially for the case of lower refractive index contrast (solid resonator case). Accordingly, we refrain from making this approximation. If, however, the mode order l is unknown, this can be a useful substitution to make, if more approximate estimates are sufficient.

3 Resonance perturbations for solid and liquid resonators

3.1 Reactive frequency shift

Monitoring of WGM frequency shifts has been shown to be a powerful route towards single molecule sensing applications [4]. Within this paradigm, the spectral position of

a WGM resonance is shifted when a molecule enters the evanescent field of the WGM sensor, by an amount proportional to the local intensity seen by the molecule and inversely proportional to the energy in the WGM resonant cavity. Using a first order perturbation approach [26, 47] it has been shown that the induced reactive resonance shift is given by

$$\frac{\Delta\omega(\mathbf{r}_p)}{\omega} \approx -\frac{\Re[\alpha]}{2} \frac{\epsilon_j |\mathbf{E}(\mathbf{r}_p)|^2}{\int_V \epsilon(\mathbf{r}) |\mathbf{E}(\mathbf{r})|^2 \, d\mathbf{r}}, \qquad (26)$$

where ω is the unperturbed WGM frequency, $\Re[\ldots]$ denotes the real part, α is the excess polarisability of the perturbing particle with respect to its host medium (with permittivity $\epsilon_j = n_j^2$), $\mathbf{E}(\mathbf{r})$ is the WGM field distribution, $\mathbf{r}_p$ denotes the position of the perturbing particle and V denotes all space. Note that since we wish to ultimately compare liquid droplet and solid resonators, we have not specified which medium the particle is in (i.e. j). For solid resonators the particle is located exterior to the microsphere ($j = 1$), whilst for liquid droplet resonators the particle is assumed to lie within the droplet ($j = 2$) as depicted in Fig. 1. Importantly, Eq. (26) is only valid within the perturbative regime, i.e., when the induced resonance shift is smaller than the linewidth of the WGM resonance. Care must hence be taken when applying Eq. (26) to, for example, plasmonic nanoparticles close to resonance, which can induce mode splitting [30]. Asymptotic results which will follow from Eq. (26) possess the same restriction.

Examination of the denominator in Eq. (26) reveals that it can be immediately recast in terms of the mode energy U_{lmp}^ν. Determination of the induced resonance shifts hence now only requires evaluation of the excess particle polarisability and the local WGM field experienced by the particle. The latter follows from Eqs. (2) and (3), whilst calculation of the former is a relatively simple task when considering spherical particles. Within the quasi-static limit, for example, the well-known formula $\alpha = 4\pi a^3 (\epsilon_p - \epsilon_j)/(\epsilon_p + 2\epsilon_j)$ can be used, where a and ϵ_p are the radius and permittivity of the particle respectively. For larger particles, however, retardation effects become more prominent such that the more accurate Mie polarisability $\alpha = -6\pi c^3 i T_1^E/(\omega^3 n_j^3)$, where T_1^E is the electric dipole element of the associated T-matrix, should be used [48]. Due to material absorption the polarisability is, in general, complex as can be seen in Table 1, which lists the complex (Mie) polarisability of a number of particles, in air, for reference purposes.

To allow further analytic results to be found, we now restrict our attention to fundamental WGMs (i.e. $l = |m|$) which are strongly confined to the equatorial plane ($z = 0$) of the resonator, and assume that the perturbing particle lies within this plane. In this case $\mathbf{E}(\mathbf{r}) = \mathbf{E}_{llp}^\nu(\mathbf{r})$ such that, using the relations $\frac{\partial}{\partial\theta} Y_{ll}(\theta, \phi) = \frac{l}{\tan\theta} Y_{ll}(\theta, \phi)$ and $Y_{ll}(\theta, \phi) = (-1)^l \left[(2l+1)/(4\pi(2l)!) \right]^{1/2} (2l-1)!! \sin^l \theta \exp[il\phi]$, it follows

$$\frac{\Delta\omega^\nu(\mathbf{r}_p)}{\omega} \approx -\frac{\Re[\alpha]}{4\pi^{3/2}} \frac{n_j^2}{n_2^2} \frac{|A_j^\nu|^2 [f_l^j(n_j k r_p)]^2}{(1+\mathcal{R}^\nu) I_2^\nu} \frac{l\,\Gamma(l+3/2)}{\Gamma(l+2)} \mathcal{F}_l^\nu(r_p), \qquad (27)$$

where the l factors have been rewritten in terms of the Gamma function $\Gamma(x)$ for reasons that will become apparent below, and

$$\mathcal{F}_l^\nu(r_p) = \begin{cases} 1 & \text{for TE modes} \\ \frac{1}{r_p^2}\left[(l+1)^2 + \left(1 + \frac{f_l^{j\prime}(n_j k r_p)}{f_l^j(n_j k r_p)}\right)^2 \right] & \text{for TM modes} \end{cases}. \qquad (28)$$

To compare liquid droplet and solid resonators, we consider the particle induced reactive shift for binding of a particle on the interior ($r_p = R_- = R - \delta$, where

Table 1. Polarisability of silver, gold, silica and polystyrene spherical particles of radius 5 and 50 nm at wavelengths of 405, 670, 1080 and 1560 nm. * Denotes values are determined from extrapolated values of the refractive index, whilst a hyphen (-) denotes negligible values. The plasmon resonance of silver 5 nm (50 nm) particles lies at 369 nm (417 nm). Similarly, the plasmon resonance of gold particles lies at 507 nm (527 nm). The refractive indices for silver and gold were determined using the Lorentz-Drude model detailed in [49]. Data for silica and polystyrene were taken from [50] and [51] respectively.

Particle material	λ (nm)	5 nm radius $\Re[\alpha]$ (nm^3)	$\Im[\alpha]$ (nm^3)	$|\alpha|^2$ ($10^6\,\mathrm{nm}^6$)	50 nm radius $\Re[\alpha]$ ($10^6\,\mathrm{nm}^3$)	$\Im[\alpha]$ ($10^3\,\mathrm{nm}^3$)	$|\alpha|^2$ ($10^{12}\,\mathrm{nm}^6$)
Silver	1560	1616	3.680	2.614	1.655	13.53	2.741
	1080	1672	7.294	2.797	1.760	40.86	3.099
	670	1893	26.82	3.585	2.192	252.0	4.866
	405	4325	1063	19.84	-0.1195	3851	1.485
Gold	1560	1622	6.150	2.629	1.661	16.26	2.758
	1080	1686	10.47	2.843	1.776	45.10	3.156
	670	2031	88.47	4.134	2.371	383.7	5.770
	405	1399	927.4	2.816	0.7069	1357	2.341
Silica	1560	417.2	-	0.1740	0.4173	-	0.1742
	1080	421.7	-	0.1778	0.4220	-	0.1781
	670	427.0	-	0.1823	0.4272	-	0.1826
	450	438.0	-	0.1918	0.4306	-	0.1868
Poly-styrene	1560*	594.0	-	0.3528	0.5964	-	0.3557
	1080	596.6	-	0.3559	0.6015	-	0.3618
	670	655.9	-	0.4302	0.6723	-	0.4523
	405	822.2	-	0.6761	0.8825	-	0.8042

δ is infinitesimally small) and the exterior ($r_p = R_+ = R + \delta$) surface respectively. Resonator size, R, and the resonance frequency ω are held fixed for fairer comparison. Consequently, the WGM excited in droplet and solid resonators will be of a different order l by virtue of the differing refractive indices. It should be noted that l must be discrete, such that for fixed R and ω a WGM resonance will not exist in general. However, for large spheres (for which the asymptotic treatment given here is valid), the discrete spectrum of WGMs becomes densely packed, such that for our purposes it is sufficient to consider a continuum of resonances. Accordingly, from Eq. (27) we find

$$\frac{\Delta\omega_d(R_-)}{\Delta\omega_s(R_+)} = \frac{\Re[\alpha_d]}{\Re[\alpha_s]}\frac{l_d}{l_s}\frac{\Gamma(l_d+\frac{3}{2})\Gamma(l_s+2)}{\Gamma(l_s+\frac{3}{2})\Gamma(l_d+2)}\frac{n_{2s}^2}{n_{1s}^2}\frac{(1+\mathcal{R}_s^\nu)}{(1+\mathcal{R}_d^\nu)}\frac{\mathcal{F}_{l_d}^\nu(R)}{\mathcal{F}_{l_s}^\nu(R)}\frac{I_{2s}^\nu}{I_{2d}^\nu}\frac{j_l^2(z_{2d})}{|A_{1s}^\nu|^2 y_l^2(z_{1s})} \quad (29)$$

where the subscripts s and d have been introduced to denote the solid and droplet resonator cases respectively. For WGMs, however, $l \gg 1$ such that we can apply the asymptotic form of the Gamma function $\Gamma(az+b) \sim \sqrt{2\pi}\exp[-az](az)^{az+b-1/2}$ from which we find

$$\frac{l_d}{l_s}\frac{\Gamma(l_d+\frac{3}{2})\Gamma(l_s+2)}{\Gamma(l_s+\frac{3}{2})\Gamma(l_d+2)} \approx \sqrt{\frac{l_d}{l_s}}\,. \quad (30)$$

We thus arrive at the relative reactive shifts

$$\frac{\Delta\omega_d(R_-)}{\Delta\omega_s(R_+)} = \frac{\Re[\alpha_d]}{\Re[\alpha_s]}\sqrt{\frac{l_d}{l_s}}\frac{n_{2d}^2}{n_{1s}^2}\frac{(1+\mathcal{R}_s^{\mathrm{TE}})}{(1+\mathcal{R}_d^{\mathrm{TE}})}\frac{n_{2s}^2-n_{1s}^2}{n_{2d}^2-n_{1d}^2} \quad (31)$$

for TE modes and

$$\frac{\Delta\omega_d(R_-)}{\Delta\omega_s(R_+)} = \frac{\Re[\alpha_d]}{\Re[\alpha_s]} \sqrt{\frac{l_d}{l_s}} \frac{n_{1d}^2}{n_{2s}^2} \frac{(1+\mathcal{R}_s^\nu)}{(1+\mathcal{R}_d^\nu)} \frac{n_{2s}^2 - n_{1s}^2}{n_{2d}^2 - n_{1d}^2} \frac{n_{1d}^2}{n_{1s}^2} \frac{[l_s(l_s+1)(n_{2s}^2+n_{1s}^2)-n_{2s}^2 z_{1s}^2]}{[l_d(l_d+1)(n_{2d}^2+n_{1d}^2)-n_{2d}^2 z_{1d}^2]}$$

$$\times \left[(l_d+1)^2 + \left(1+\frac{j'_{l_d}(z_{2d})}{j_{l_d}(z_{2d})}\right)^2\right] \Big/ \left[(l_s+1)^2 + \left(1+\frac{y'_{l_s}(z_{1s})}{y_{l_s}(z_{1s})}\right)^2\right] \quad (32)$$

for TM modes, where Eqs. (18) and (19) can be used to evaluate the ratios $f_l^{j'}(z)/f_l^j(z)$.

Consideration of the relative shift for particles binding to the interior surface of a droplet resonator ($r_p = R_-$), as compared to the shift induced when the particle is located at the maximum of the mode profile ($r_p = r_{\max}$), which lies slightly away from the droplet surface, also warrants our attention. Immediately from Eq. (27) it follows that

$$\frac{\Delta\omega_d(r_{\max})}{\Delta\omega_d(R_-)} = \frac{j_{l_d}^2(n_{2d}k r_{\max})}{j_{l_d}^2(n_{2d}kR)} \frac{\mathcal{F}_{l_d}^\nu(r_{\max})}{\mathcal{F}_{l_d}^\nu(R)} . \quad (33)$$

To evaluate this relative shift, all that is therefore required is to determine $r_{\max}$. To do so, we recall that $j_l(z) = \sqrt{2\pi/z}J_\nu(z)$ and employ the asymptotic expansion of the Bessel function $J_\nu(z)$ in the transition region [43], which to leading order reads $J_\nu(\nu + \zeta\nu^{1/3}) \sim 2^{1/3}\nu^{-1/3}\mathrm{Ai}(-2^{1/3}\zeta)$, where $\mathrm{Ai}(z)$ is the Airy function. Noting that the radial extent, Δr of (low) radial order, p, WGMs satisfies [52]

$$\frac{\Delta r}{R} \approx \frac{1}{2}(3\pi)^{2/3}\left[\frac{p-1/4}{n_2 kR}\right]^{2/3} \ll 1, \quad (34)$$

we find the dominant behaviour of the radial wave-functions is inherited from the Bessel functions $J_\nu(z)$ as opposed to the $z^{-1/2}$ factor. With these observations our problem now becomes that of finding the maximum of $\mathrm{Ai}(z)$. A maximum in $\mathrm{Ai}(z)$ occurs when $\mathrm{Ai}'(z) = 0$, the solutions of which are well known [43]. We thus have

$$n_2 k r_{\max} = \nu_d - 2^{-1/3}\alpha'_1 \nu_d^{1/3} \quad (35)$$

where $\alpha_1 = -1.01879$ is the first zero of $\mathrm{Ai}'(z)$. The first zero is taken here since this corresponds to the global maximum of the WGM within the resonator. For the first radial order this is the only maximum, however for higher radial orders other maxima exist within the resonator (at positions given by Eq. (35) with the replacement $\alpha_1 \to \alpha_t$, $t = 1, \ldots, p$). The field intensity at these subsidiary maxima is, however, smaller than that given by Eq. (35).

As an illustrative example, Fig. 2a shows the calculated resonance shifts induced in paraffin oil droplets ($n_{2d} = 1.46215$) in air ($n_{1d} = 1$) relative to a fused silica solid resonator ($n_{2s} = 1.4439$) in water ($n_{1s} = 1.31735$) at 1560 nm, by a solid gold nanoparticle (refractive index data were taken from [49,50,53,54]). Specifically the relative shift $\Delta\omega_d(r_{\max})/\Delta\omega_s(R_+)$ was determined for TE modes using both the full perturbative integral of Eq. (26) (solid lines) and asymptotic formulae (dashed lines) derived above (Eqs. (31) and (33)) for resonators of radius ranging from 30 μm to 140 μm, corresponding to a maximum mode order of $l = 800$, for which good agreement is seen. Since the quasi-static approximation was used to determine the particle polarisability for this calculation, the particle size cancels in Eq. (31) and hence the result is independent of particle size. Naturally, this result will break down for larger particles as discussed above. From Fig. 2a it is evident that relative shifts are greater
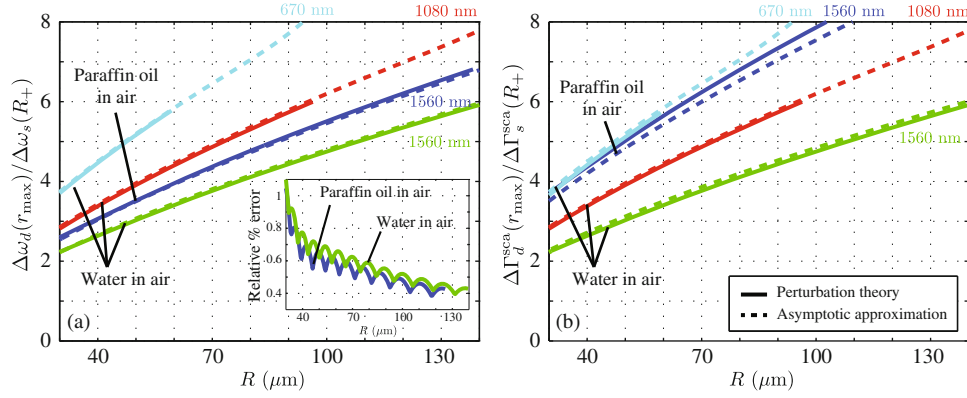
Fig. 2. (a) Comparison of relative TE resonance shifts for a paraffin oil liquid droplet resonator in air (blue) compared to a fused silica solid resonator in water at 1560 nm as found using perturbation theory (solid) and an asymptotic approximation (dashed). Green, red and cyan curves correspond to the calculated resonance shifts for a liquid water droplet in air relative to a fused silica solid resonator in water at 1560 nm, 1080 nm and 670 nm respectively. Inset depicts relative percentage error between perturbative and asymptotic calculations for paraffin and water droplets at 1560 nm. (b) As (a) except relative scattering induced line broadening is shown. All calculations assumed a gold nanoparticle and consider the first radial order, $p = 1$, WGM.

for larger spheres, as a result of the greater confinement of the mode profile within the resonator volume. Furthermore, it is important to mention that due to the nature of the asymptotic expansion made, the approximation becomes more accurate for larger mode orders, that is to say for larger spheres, as shown in the inset of Fig. 2a which plots the relative percentage error between the perturbative and asymptotic calculations for the relative resonance shift for paraffin oil droplets at 1560 nm. For the case of a paraffin oil droplet considered here, the relative resonance shift is dictated by both the relative particle polarisability and the mode distribution. Biosensing experiments are, however, frequently performed in an aqueous environment, for example using a fused silica resonator (hence motivating our choice of reference system), such that we should also consider use of water droplet resonators. Accordingly, we have also performed calculations for water droplets in air, which are also shown in Fig. 2 for wavelengths of 670 nm, 1080 nm and 1560 nm. For computational reasons the range of radii for perturbation theory calculations was limited to mode orders corresponding to $l \leq 800$, however good agreement is again evident. In this special case, the polarisability factor $\Re[\alpha_d]/\Re[\alpha_s] = 1$, such that it is only the relative mode distributions that dictate the relative resonance shift.

Finally, we briefly note that, in general, relative frequency shifts will be smaller than that predicted by Eq. (33), since for liquid droplet resonators the particle can be located anywhere within the sensing volume and not necessarily at the mode maximum. Consequently the particle experiences a weaker local field intensity in turn reducing the induced frequency shift. As shown in Fig. 3a, for $p = 1, 2$ and 3 WGMs, the relative resonance shift follows the mode profile. Mode maxima, as predicted by Eq. (35) are also shown in Fig. 3a by vertical dashed black lines, from which only very small discrepancies from the maximum position predicted by consideration of the full electromagnetic modes is apparent.
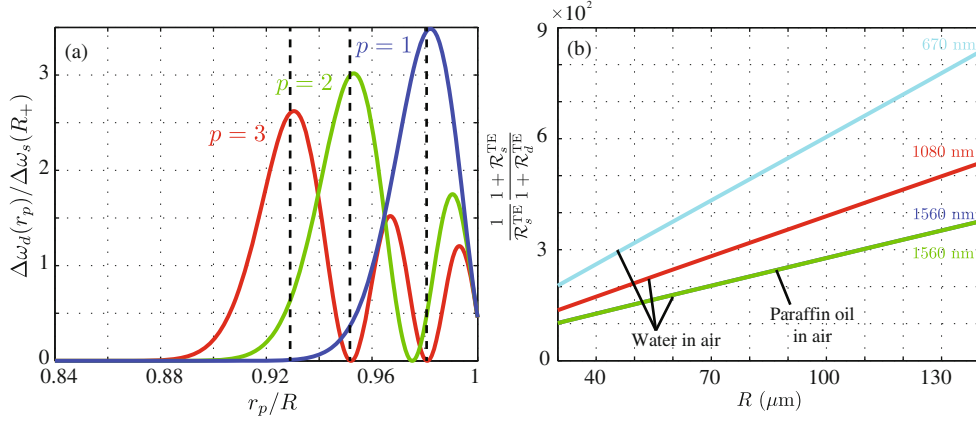
Fig. 3. (a) Comparison of the relative TE resonance shifts for a liquid water droplet in air as compared to a fused silica solid resonator in water at 1080 nm for the $p = 1, 2, 3$ WGMs as a function of particle position within the droplet resonator (normalised to the resonator radius). (b) Resonator size dependence of the concentration sensitivity gain factor $(1/\mathcal{R}_s^{\mathrm{TE}})(1 + \mathcal{R}_s^{\mathrm{TE}})/(1 + \mathcal{R}_d^{\mathrm{TE}})$ for the same resonator configurations of Fig. 2. Note that sensitivity gain factors for the paraffin oil and water droplet are near coincident in this plot.

3.2 Line broadening and mode splitting

The linewidth, Γ, of a WGM resonance, here expressed in angular frequency units, is dictated by losses inherently present in the system, the most dominant of which are radiation, absorption and scattering losses i.e. $\Gamma = \Gamma^{\mathrm{rad}} + \Gamma^{\mathrm{abs}} + \Gamma^{\mathrm{sca}}$. An equivalent, common parameterisation used is that of the Q factor. Noting $Q = \omega/\Gamma$, we can hence write $Q^{-1} = Q_{\mathrm{rad}}^{-1} + Q_{\mathrm{abs}}^{-1} + Q_{\mathrm{sca}}^{-1}$. Interaction between a WGM and a particle, however, introduces additional losses, hence inducing line broadening in addition to reactive resonance shifts discussed above. Measurements of such linewidth changes are currently emerging as a complementary sensing mechanism to reactive shifts [55]. Accordingly, following earlier derivations, we now give expressions for the relative broadening for a droplet versus a solid resonator.

To begin we note that particle induced scattering losses give rise to a change $\Delta\Gamma^{\mathrm{sca}}$ in the linewidth (full-width half maximum) of a resonance, given by [55]

$$\frac{\Delta\Gamma^{\mathrm{sca}}(\mathbf{r}_p)}{\omega} \approx \frac{n_j^5 \omega^3}{6\pi c^3} \frac{|\alpha|^2 |\mathbf{E}(\mathbf{r}_p)|^2}{\int_V \epsilon(\mathbf{r}) |\mathbf{E}(\mathbf{r})|^2 d\mathbf{r}} \ . \tag{36}$$

For absorption losses in the particle the broadening is similarly given by

$$\frac{\Delta\Gamma^{\mathrm{abs}}(\mathbf{r}_p)}{\omega} \approx \frac{\epsilon_j \Im[\alpha] |\mathbf{E}(\mathbf{r}_p)|^2}{\int_V \epsilon(\mathbf{r}) |\mathbf{E}(\mathbf{r})|^2 d\mathbf{r}} \ . \tag{37}$$

where $\Im[\ldots]$ denotes the imaginary part. Particles possessing optical gain can, interestingly, also result in line sharpening. Given Eqs. (26), (36) and (37) it immediately follows that

$$\frac{\Delta\omega_d(R_-)}{\Delta\omega_s(R_+)} = \frac{n_{1s}^3}{n_{2d}^3} \frac{|\alpha_s|^2}{|\alpha_d|^2} \frac{\Re[\alpha_d]}{\Re[\alpha_s]} \frac{\Delta\Gamma_d^{\mathrm{sca}}(R_-)}{\Delta\Gamma_s^{\mathrm{sca}}(R_+)} = \frac{\Im[\alpha_s]}{\Im[\alpha_d]} \frac{\Re[\alpha_d]}{\Re[\alpha_s]} \frac{\Delta\Gamma_d^{\mathrm{abs}}(R_-)}{\Delta\Gamma_s^{\mathrm{abs}}(R_+)} \tag{38}$$

allowing our earlier results to be employed to consider the relative broadening effects in liquid droplets. An example of the calculated relative scattering induced broadening for the same systems as discussed above is shown in Fig. 2b. We note, that for the case of a liquid water droplet (relative to a fused silica solid resonator in water), the relative broadening is equal to the relative frequency shift, since the prefactor in Eq. (38) is unity, that is to say the relative broadening is only a consequence of the differing mode profiles. This arises as a consequence of the particle host medium being the same in both cases.

Splitting of WGMs represents a further sensing modality that has been used, for example, in high Q resonators to detect and characterise single nanoparticles and viruses [56]. In this vein, we briefly note that expressions governing particle induced mode splitting [56] are of identical form to Eq. (26), such that Eqs. (31) and (32) can also be used to describe the relative frequency splitting in mode splitting based sensing modalities.

3.3 Nanoparticle concentration

Results derived thus far have concentrated on the changes induced in a WGM resonance by the presence of a single particle within the mode volume. In practice, whilst possible, the detection of a single particle is experimentally difficult. Moreover, in many important applications the concentration of particles in a solution is sought. Liquid droplet resonators present a convenient platform for such concentration measurements because the resonator volume can act as the particle solute [34]. Within this context, we thus consider resonance perturbations in the presence of multiple particles from an average point of view. When considering multiple particles, analysis naturally becomes more involved such that results in this section merely aim to provide an indication as to potential sensitivity gains in concentration measurements in liquid droplet resonators as compared to the solid resonator case. Potential sources of deviation from these results will be discussed in Sect. 4.

From a microscopic point of view, the concentration, ρ, of a solution is dictated by the number of particles N_ρ within a given volume V_ρ viz. $\rho = N_\rho/V_\rho$. Induced resonance shifts and broadening are then the consequence of the aggregate effect from all particles, which shall be assumed to be identical. Taking the reactive shift as an illustrative example, the total resonance shift is hence given by

$$\frac{\Delta\omega_\rho}{\omega} \approx -\frac{\Re[\alpha]}{2} \frac{\epsilon_j \sum_{i=1}^{N_\rho} |\mathbf{E}(\mathbf{r}_i)|^2}{\int_V \epsilon(\mathbf{r}) |\mathbf{E}(\mathbf{r})|^2 \, d\mathbf{r}}, \tag{39}$$

where $\mathbf{r}_i$ denotes the position of the ith particle and all particles are assumed to lie within the same medium. Note that Eq. (39) also implicitly neglects coupling between particles, however, this is generally weak for small Rayleigh scatterers and low concentrations. Knowledge of individual particle positions, required for evaluation of Eq. (39) is unfeasible in reality, however, insight can be gained by performing ensemble averaging over all possible particle configurations. In the simplest case, we assume that particles are uniformly distributed across the sensing volume (i.e. we neglect any possible trapping forces). Under these conditions we have

$$\frac{\langle\Delta\omega_\rho\rangle}{\omega} \approx -\frac{\Re[\alpha]}{2} \frac{\epsilon_j \sum_{i=1}^{N_\rho} \langle|\mathbf{E}(\mathbf{r}_i)|^2\rangle}{\int_V \epsilon(\mathbf{r}) |\mathbf{E}(\mathbf{r})|^2 \, d\mathbf{r}} = -\frac{\Re[\alpha]}{2} \frac{N_\rho}{V_\rho} \frac{\epsilon_j \int_{V_\rho} |\mathbf{E}(\mathbf{r})|^2 \, d\mathbf{r}}{\int_V \epsilon(\mathbf{r}) |\mathbf{E}(\mathbf{r})|^2 \, d\mathbf{r}} \tag{40}$$

where the angular brackets denote ensemble averaging $\langle\cdots\rangle = (1/V_\rho) \int_{V_\rho} \cdots d\mathbf{r}$, the $1/V_\rho$ factor originates from normalisation of the probability distribution function
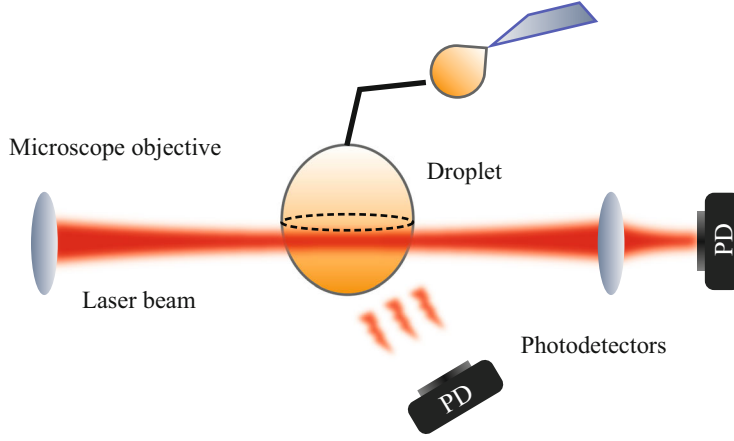
Fig. 4. Sketch of the experimental setup. The droplet resonator is created from a small liquid sample at the tip of an optical fiber or capillary. A tunable laser is focused close to surface of the droplet using a microscope objective so as to excite whispering-gallery modes. The directly transmitted and scattered light are collected by fast photodiodes.

governing each particle's position and the factor N_ρ arises since the particles are assumed to be identical. Examination of the numerator of Eq. (40), and noting that the relevant sensing volume for droplet (solid) resonators is the interior (exterior) domain, reveals that our earlier derivations can be employed once more. In particular we find

$$\frac{\langle \Delta\omega_{\rho,d} \rangle}{\omega} \approx -\rho\frac{\Re[\alpha_d]}{2}\frac{1}{1+\mathcal{R}_d^\nu} \text{ and } \frac{\langle \Delta\omega_{\rho,s} \rangle}{\omega} \approx -\rho\frac{\Re[\alpha_s]}{2}\frac{\mathcal{R}_s^\nu}{1+\mathcal{R}_s^\nu}, \qquad (41)$$

for droplet and solid resonators respectively. Defining the concentration sensitivity of a resonator as $\frac{d}{d\rho}\langle \Delta\omega_\rho \rangle$, we find that liquid droplet resonators are significantly more sensitive than solid resonators since $\mathcal{R}^\nu \ll 1$. The sensitivity gain γ_ρ follows as

$$\gamma_\rho = \frac{\frac{d}{d\rho}\langle \Delta\omega_{\rho,d} \rangle}{\frac{d}{d\rho}\langle \Delta\omega_{\rho,s} \rangle} = \frac{1}{\mathcal{R}_s^\nu}\frac{1+\mathcal{R}_s^\nu}{1+\mathcal{R}_d^\nu}\frac{\Re[\alpha_d]}{\Re[\alpha_s]} \approx \frac{1}{\mathcal{R}_s^\nu}\frac{\Re[\alpha_d]}{\Re[\alpha_s]} \ . \qquad (42)$$

Analogous results also follow for the concentration dependence of scattering induced line broadening with the replacement $\Re[\alpha] \rightarrow -2n_j^3\omega^3|\alpha|^2/(6\pi c^3)$ and for absorption broadening with the replacement $\Re[\alpha] \rightarrow -2\Im[\alpha]$. We also note that these results are independent of azimuthal order m. In Fig. 3b we have plotted the gain factor $(1/\mathcal{R}_s^{\text{TE}})(1+\mathcal{R}_s^{\text{TE}})/(1+\mathcal{R}_d^{\text{TE}})$ for both paraffin oil and water droplet resonators as a function of resonator size. Typical enhancement factors are on the order of two to three orders of magnitude for the range of resonator sizes considered here, with greater sensitivity gains observed for larger resonators. This behaviour is, again, a consequence of the greater confinement of the mode volume for larger resonators.

4 Experimental results

We have theoretically demonstrated that liquid droplet WGM resonators represent a highly sensitive platform for measurements of solute concentration. To demonstrate this capability we have performed experiments, whereby WGM line broadening was

investigated, as the concentration of gold nanoparticles within the resonator was varied. Nanoparticle induced reactive shifts were not considered in this work since such measurements can suffer large noise levels arising from the dynamic motion of particles within the sensor volume. Furthermore, at present, we possess no means to easily deliver particles from the external environment or from the liquid channel forming the droplet to the sensing region. Figure 4 shows a schematic of the experimental setup used wherein a visible distributed feedback diode laser (50 MHz linewidth) emitting at ~ 663 nm is used to interrogate a paraffin oil droplet resonator. The laser source was driven by a precision temperature controller and low-noise current generator. Liquid droplets were suspended, under the force of gravity, from the tip of a thin wire and held by means of surface tension [34]. The droplet holder was fixed directly to the optical table without any enclosing chamber. A microscope objective was then used to focus the laser beam and the droplet carefully positioned within the beam using a manual xyz micrometer translation stage, such that the focused light was incident tangential to, but just beyond the droplet surface. In this manner excitation of WGMs within the droplet could be achieved. Additional objective lenses were used to collect and focus the light transmitted and scattered by the droplet resonator onto fast photodiodes. Evaporation effects were found to be negligible for oil droplets, however, these can be an issue for water droplets if there is a driving force towards evaporation, i.e. the vapour pressure of the droplet in its environment is lower than the equilibrium pressure. Evaporation of the droplet can, however, be prevented by thermally and chemically equilibrating the droplet with its surrounding vapour, for example, by placing it within a closed environment.

By recording the power of the light scattered by the droplets as the laser frequency is varied (by means of a 40 ms current scan), the scattering spectrum of the droplet resonator can be acquired. An example of a typical observed WGM spectrum, for a 500 μm radius paraffin oil droplet is shown in Fig. 5a. Two systems of modes are visible with differing finesse. The narrow peaks (labelled 1–4 in Fig. 5a) represent WGMs with a Q-factor $> 10^6$. Since liquid paraffin is largely transparent at visible wavelengths, absorption losses in the cavity are small, such that the ultimate limit to the mode linewidth is primarily determined by scattering effects due to thermal fluctuations of the liquid surface. We note that we observe modes in the spectrum with a higher Q, arising from lower order radial p modes, however, their transmission and scattering signals are weak and noisy since the laser frequency jitter becomes comparable to the mode linewidth. Utilisation of these higher Q modes is to be the subject of future investigations.

To study the concentration sensitivity of droplet resonators we diluted a paraffin oil mixture containing gold nanoparticles (atomic density in solution 13.41×10^{16} atoms/cc), with average radius of ~ 1.8 nm and plasmon resonance located at ~ 550 nm, with pure paraffin oil. Four different sample concentrations were prepared ranging from $\approx 3\%$–17% by volume, from which droplet resonators were subsequently made. The WGM spectrum was then acquired for each droplet using a wavelength calibrated laser scan as described above, and the linewidth of a single WGM extracted via Lorentzian fitting. Our results are shown in Fig. 5b whereby a good agreement with a linear fit (coefficient of determination $R^2 = 0.99237$) is evident. Noting the experimentally observed slope of 0.093 GHz/%, a maximum linewidth noise of 0.025 GHz and our detection bandwidth of 44 kHz, we find a noise-equivalent fluctuation of 10^{-4} GHz/Hz$^{-1/2}$ leading to a signal response limit of 360 pM/Hz$^{-1/2}$. Given the small size of our analyte molecules, this value represents a good level of sensitivity if compared to the performance of existing sensors.

Mode broadening exhibited in Fig. 5b is larger than that predicted by the results presented in Sect. 3.3. For example, the theoretical broadening arising from absorption yields a slope of ~ 0.017 GHz/%, whilst consideration of scattering losses yields
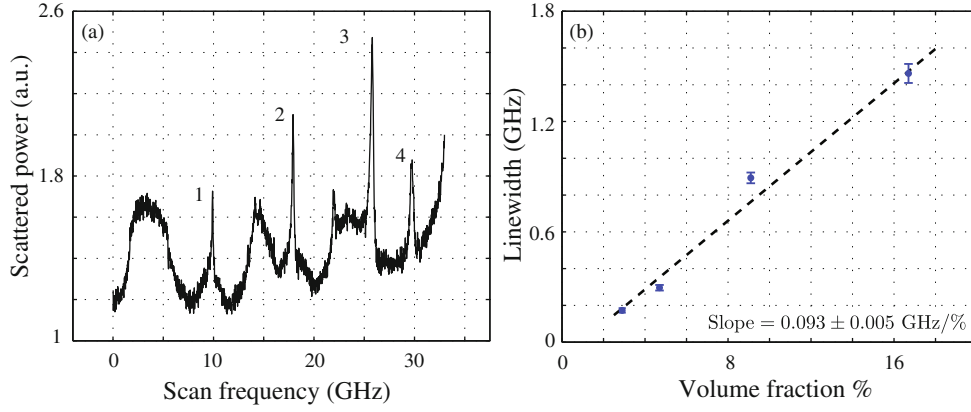
Fig. 5. (a) Typical scattering spectrum of a $\approx 500\ \mu$m radius liquid paraffin droplet cavity, exhibiting high Q WGMs (labelled peaks). (b) Measured linewidth of WGM labelled 2 in (a) (blue data points with error bars) as a function of volume concentration of paraffin oil containing gold NPs. Dashed line shows a linear fit with fit parameters given in the accompanying table. All measurements were performed using a laser wavelength scan centered at ≈ 663 nm.

$\sim 0.8 \times 10^{-6}$ GHz/%. Discrepancies are attributed to a number of different causes, which we discuss briefly here. Firstly, we recall that in Sect. 3.3 trapping effects were neglected. Given the relatively strong field gradients associated with WGMs, however, this assumption is unlikely to hold. Accordingly, larger resonance perturbations (e.g. reactive shift and broadening) would be expected since nanoparticles are more likely to be located in stronger regions of the mode. In reality, particles can also be trapped at the droplet surface by surface tension, such that a surface scattering contribution arises in addition to the bulk contribution discussed above. For example, assuming a uniform distribution of particles over the surface S_σ, we find for a TE mode

$$\frac{\langle \Delta\omega_{\sigma,d}\rangle}{\omega} \approx -\sigma \frac{\Re[\alpha]}{R}\frac{1}{1+\mathcal{R}^\nu}\frac{n_2^2}{(n_2^2 - n_1^2)}, \tag{43}$$

where $\sigma = N_\sigma/S_\sigma$ is the surface number density and N_σ is the number of particles on the droplet surface. We note that this is fully analogous to results previously derived for monolayers on the surface of solid resonators [47]. The average surface and bulk scattering terms for droplet resonators are, therefore, of equal magnitude (i.e. $\langle \Delta\omega_{\sigma,d}\rangle = \langle \Delta\omega_{\rho,d}\rangle$) when

$$\frac{N_\sigma}{N_T} = \left[1 + \frac{2}{3}\frac{n_2^2}{(n_2^2 - n_1^2)}\right]^{-1} \triangleq \mathcal{P}, \tag{44}$$

where $N_T = N_\sigma + N_\rho$ is the total number of particles in the droplet, such that N_σ/N_T represents the fraction of particles trapped on the surface. Noting $n_1 < n_2$ we also find, in general, that $\mathcal{P} \leq 0.6$. Similar results follow for TM modes, but are omitted for brevity. For a paraffin oil droplet in air this corresponds to a ratio $\mathcal{P} \approx 0.45$ at 663 nm, whilst for a water droplet we find $\mathcal{P} \approx 0.4$. We also note that the average resonance shift (and mode broadening) per particle is larger for surface scattering than volume scattering when $n_2/n_1 \leq \sqrt{3}$, as follows from Eqs. (42) and (43), a condition which is met in our experiments.

Additionally, nanoparticle size dispersion within the sample, can give rise to larger experimental mode broadening, since absorption and scattering losses scale as the

nanoparticle radius to the third and sixth power respectively. This nonlinear dependence implies that linewidth measurements are more sensitive to larger particles, such that broadening will be dominated by larger particles in our sample. In this vein, the analytic treatment of Sect. 3.3 becomes more involved because ensemble averaging must also be performed over the particle size distribution. Adopting a normal distribution for particle size with mean a_0 and variance σ^2, we can use the quasi-static approximation for the particle polarisability and find

$$\langle \alpha \rangle = \left(1 + \frac{3\sigma^2}{a_0^2}\right) \alpha_0, \quad \text{and} \quad \langle |\alpha|^2 \rangle = \left(1 + \frac{15\sigma^2 \left(a_0^4 + 3a_0^2\sigma^2 + \sigma^4\right)}{a_0^6}\right) |\alpha_0|^2 \quad (45)$$

where $\alpha_0 = 4\pi a_0^3 (\epsilon_p - \epsilon_j)/(\epsilon_p + 2\epsilon_j)$. Assuming particle size and position to be independent variables, expressions given in Eq. (45) can be used in Eq. (40) and subsequent formulae (and the broadening equivalents). For our case, for which $\sigma \approx 1\,\text{nm}$, such calculations give slightly better agreement, with the theoretical broadening arising from absorption now yielding a slope of ~ 0.029 GHz/%, whilst consideration of scattering losses yields $\sim 10 \times 10^{-6}$ GHz/%.

Deviations of the resonator geometry from a spherical shape can also give rise to discrepancies between experiment and theory. In this vein, however, it is worth mentioning that linewidth measurements are relatively robust to shape perturbations of the resonator, such that we can neglect the slight ellipticity of the resonator arising as a result of gravity acting on the free hanging droplet. The same can not be said, however, for measurements of WGM reactive shifts.

Finally, in the treatment of Sect. 3.3 we considered an ensemble average of a spatial random process. It is important to note, however, that particles in solution will also be undergoing random dynamical motion (e.g. due to diffusion). Accordingly, the resonance shift described by Eq. (39) (as well as the associated broadening) exhibit transient behaviour during the course of a single measurement. Resonance frequency "jitter" of this nature, in turn, can give rise to an apparent resonance broadening, dependent on the time resolution of the measurement, in addition to that given by scattering and absorption losses [27]. Due to the inhomogenous origin of this effect, the resonance profile could exhibit a Gaussian lineshape when such "transit time" broadening dominates. Potential trapping forces within the resonator can, however, mitigate against such dynamical perturbations and act to increase the interaction between analyte particles and the WGM, thus increasing the overall sensor sensitivity. As demonstrated in [34,57] use of ring-down cavity spectroscopy (or variants thereof) can also help avoid this effect, such that the average linewidth (and hence broadening), can be determined independent of such frequency noise and with superior detection performance. Naturally, cavity ring-down spectroscopy also permits a direct measurement of the optical loss in each WGM and thereby allows for a simple measurement of absorption and scattering cross sections [58].

5 Conclusions

In this work we have discussed and assessed the potential of liquid droplet WGM resonators as an alternative to solid microspheres in nanoparticle sensing applications. Frequently, WGM sensors rely on detection of resonance shifts induced by an analyte particle (or particles) of interest. In this vein, we thus derived improved asymptotic expressions for particle induced resonance shifts of TE and TM modes in solid and droplet resonators. Larger shifts were shown to originate for the droplet case, by virtue of the stronger field amplitudes experienced by the perturbing particle within the resonator. Moreover, enhancement factors were seen to increase with resonator

size, due to the greater mode confinement that results. Due to the increasing use of alternative sensing schemes, such as those based on line broadening or mode splitting, we extended our derivations to consider these cases. Similar trends were also found. As a corollary of our derivations we found asymptotic formulae describing the relative fraction of mode energy stored outside and inside a WGM resonator, a quantity which was found to play a crucial role in the potential sensitivity gains achievable when making WGM based concentration measurement in liquid droplets. Finally, as a demonstration of the particle sensing capabilities of liquid droplet resonators we have also presented experimental results whereby the line broadening induced by a gold nanoparticle solution of differing concentrations was investigated.

References

1. V.S. Ilchenko, A.B. Matsko, IEEE J. Sel. Top. Quant. **12**, 15 (2006)
2. A.B. Matsko, V.S. Ilchenko, IEEE J. Sel. Top. Quant. **12**, 3 (2006)
3. K.J. Vahala, *Optical Microcavities* (World Scientific: Singapore, 2004)
4. F. Vollmer, S. Arnold, Nat. Meth. **5**, 591 (2008)
5. D.W. Vernooy, V.S. Ilchenko, H. Mabuchi, E.W. Streed, H.J. Kimble, Opt. Lett. **23**, 247 (1998)
6. V.B. Braginsky, M.L. Gorodetsky, V.S. Ilchenko, Phys. Lett. A **137**, 393 (1989)
7. I.S. Grudinin, A.B. Matsko, A.A. Savchenkov, D. Strekalov, V.S. Ilchenko, L. Maleki, Opt. Commun. **265**, 33 (2006)
8. G.S. Murugan, J.S. Wilkinson, M.N. Zervas, Opt. Express **17**, 11916 (2009)
9. I.M. White, H. Oveys, X. Fan, Opt. Lett. **31**, 1319 (2008)
10. T. Ling, L.J. Guo, Opt. Express **15**, 17424 (2007)
11. D.K. Armani, T.J. Kippenberg, S.M. Spillane, K.J. Vahala, Nature **42**, 925 (2003)
12. M.L. Gorodetsky, A.A. Savchenkov, V.S. Ilchenko, Opt. Lett. **21**, 453 (1996)
13. A. Serpenguzel, S. Arnold, G. Griffel, Opt. Lett. **20**, 654 (1995)
14. A. Yalcin, K.C. Popat, J.C. Aldridge, T.A. Desai, J. Hryniewicz, N. Chbouki, B.E. Little, O. King, V. Van, S. Chu, D. Gill, M. Anthes-Washburn, M.S. Unlu, IEEE J. Sel. Top. Quant. **12**, 148 (2006)
15. T. Beck, S. Schloer, T. Grossmann, T. Mappes, H. Kalt, Opt. Express **20**, 22012 (2012)
16. Y. Yang, J. Ward, S. Chormaic, Opt. Express **22**, 6881 (2014)
17. A. Kiraz, A. Sennaroglu, S. Doganay, M.A. Dundar, A. Kurt, H. Kalaycioglu, A.L. Demirel, Opt. Commun. **276**, 145 (2007)
18. A. Kiraz, S.C. Yorulmaz, M. Yorulmaz, A. Sennaroglu, Photonic. Nanostruct. **7**, 186 (2009)
19. M. Cai, G. Hunziker, K.J. Vahala, IEEE Photon. Technol. Lett. **11**, 686 (1999)
20. G.S. Murugan, J.S. Wilkinson, M.N. Zervas, Opt. Lett. **35**, 1893 (2010)
21. J.U. Fürst, D.V. Strekalov, D. Elser, A. Aiello, U.L. Andersen, Ch. Marquardt, G. Leuchs, Phys. Rev. Lett. **106**, 113901 (2011)
22. A.T. Rosenberger, Opt. Express **15**, 12959 (2007)
23. A.T. Rosenberger, J. Rezac, Proc. SPIE **4265**, 102 (2001)
24. F. Vollmer, D. Braun, A. Libchaber, M. Khoshsima, I. Teraoka, S. Arnold, Appl. Phys. Lett. **80**, 4057 (2002)
25. F. Vollmer, S. Arnold, D. Keng, Proc. Nat. Acad. Sci. USA **105**, 20701 (2008)

26. S. Arnold, M. Khoshsima, I. Teraoka, S. Holler, F. Vollmer, Opt. Lett. **28**, 272 (2003)
27. M.R. Foreman, W.-L. Jin, F. Vollmer, Opt. Express **22**, 5491 (2014)
28. J. Knittel, T.G. McRae, K.H. Lee, W.P. Bowen, Appl. Phys. Lett. **97**, 123704 (2010)
29. T. Lu, H. Lee, T. Chen, S. Herchak, J.-H. Kim, S.E. Fraser, R.C. Flagan, K.J. Vahala, Proc. Nat. Acad. Sci. USA **108**, 5976 (2011)
30. M.R. Foreman, F. Vollmer, New. J. Phys. **15**, 083006 (2013)
31. V.R. Dantham, S. Holler, C. Barbre, D. Keng, V. Kolchenko, S. Arnold, Nano. Lett. **13**, 3347 (2013)
32. M.D. Baaske, M.R. Foreman, F. Vollmer, Nat. Nanotech. (2014), doi: 10.1038/nnano. 2014.180
33. M. Baaske, F. Vollmer, Chem. Phys. Chem. **13**, 427 (2012)
34. S. Avino, A. Krause, P. Malara, R. Zullo, A. Giorgini, P. De Natale, H.P. Loock, G. Gagliardi, Adv. Opt. Mat. (in press) (2014)
35. N. Gaber, M. Malak, X. Yuan, K.N. Nguyen, P. Basset, E. Richalot, D. Angelescu, T. Bourouina, Lab Chip **13**, 826 (2013)
36. M. Born, E. Wolf, *Principles of Optics*, 7th ed. (Cambridge University Press, Cambridge, 1980)
37. C.F. Bohren, D.R. Huffman, *Absorption and scattering of light by small particles* (John Wiley & Sons, Inc, Weinheim, 1998)
38. I. Teraoka, S. Arnold, J. Opt. Soc. Am. B **20**, 1937 (2003)
39. H.M. Lai, P.T. Leung, K. Young, P.W. Barber, S.C. Hill, Phys. Rev. A **41**, 5187 (1990)
40. D.Q. Chowdhury, S.C. Hill, M.M. Mazumder, IEEE J. Quantum Elect. **29**, 2553 (1993)
41. J.A. Stratton, *Electromagnetic theory* (McGraw-Hill, New-York, 1941)
42. C.C. Lam, P.T. Leung, K. Young, J. Opt. Soc. Am. B **9**, 1585 (1992)
43. M. Abramowitz, I. Stegun, *Handbook of Mathematical Functions* (Dover Publications, New York, 1970)
44. S. Arnold, R. Ramjit, D. Keng, V. Kolchenko, I. Teraoka, Faraday Disc. **137**, 65 (2008)
45. B.R. Johnson, J. Opt. Soc. Am. A **10**, 343 (1993)
46. J.A. Barnes, G. Gagliardi, H.-P. Loock, *Cavity-Enhanced Spectroscopy and Sensing*, edited by G. Gagliardi and H.-P. Loock (Springer-Verlag, Berlin, 2013)
47. I. Teraoka, S. Arnold, J. Opt. Soc. Am. B **23**, 1381 (2006)
48. M.R. Foreman, F. Vollmer, Phys. Rev. A **88**, 023831 (2013)
49. A.D. Rakic, A.B. Djurisic, J.M. Elazar, M.L. Majewski, Appl. Opt. **37**, 5271 (1998)
50. I.H. Malitson, J. Opt. Soc. Am. **55**, 1205 (1965)
51. S.N. Kasarova, N.G. Sultanova, C.D. Ivanov, I.D. Nikolov, Opt. Mat. **29**, 1481 (2007)
52. S. Schiller, Appl. Opt. **32**, 2181 (1993)
53. P.R. Cooper, Appl. Opt. **21**, 3413 (1982)
54. G.M. Hale, M.R. Querry, Appl. Opt. **12**, 555 (1973)
55. L. Shao, X.-F. Jiang, X.-C. Yu, B.-B. Li, W.R. Clements, F. Vollmer, W. Wang, Y.-F. Xiao, Q. Gong, Adv. Mat. **25**, 5616 (2013)
56. J. Zhu, S.J. Özdemir, Y.-F. Xiao, L. Li, L. He, D.-R. Chen, L. Yang, Nat. Phot. **4**, 46 (2010)
57. J.A. Barnes, G. Gagliardi, H.-P. Loock, Optica **1**, 75 (2014)
58. J.A. Barnes, G. Gagliardi, H.-P. Loock, Phys. Rev. A **87**, 053843 (2013)